



Preparation of three-dimensional $\text{Ag}_3\text{PO}_4/\text{TiO}_2@\text{MoS}_2$ for enhanced visible-light photocatalytic activity and anti-photocorrosion

Ning Shao^a, Jinnan Wang^{a,*}, Dadao Wang^a, Philippe Corvini^b

^a State Key Laboratory of Pollution Control and Resource Reuse & School of the Environment Nanjing University, Nanjing 210023, China

^b School of Life Sciences, University of Applied Sciences Northwestern Switzerland, Basel 4132, Switzerland

ARTICLE INFO

Article history:

Received 17 August 2016

Received in revised form 2 November 2016

Accepted 6 November 2016

Available online 9 November 2016

Keywords:

3D $\text{Ag}_3\text{PO}_4/\text{TiO}_2@\text{MoS}_2$

Anti-photocorrosion

Visible-light photocatalytic degradation

Dyes

Antibiotics

ABSTRACT

We synthesized novel three-dimensional photocatalyst ($\text{Ag}_3\text{PO}_4/\text{TiO}_2@\text{MoS}_2$) with various content of $\text{TiO}_2@\text{MoS}_2$ by electrospinning, sequential hydrothermal reaction and chemical deposition. The optimal content of $\text{TiO}_2@\text{MoS}_2$ in $\text{Ag}_3\text{PO}_4/\text{TiO}_2@\text{MoS}_2$ composites is 3.5 wt%, and the bandgap of $\text{Ag}_3\text{PO}_4/\text{TiO}_2@\text{MoS}_2$ (3.5 wt%) (1.85 eV) was much lower than that of pure Ag_3PO_4 (2.45 eV). Due to high conductivity of $\text{TiO}_2@\text{MoS}_2$ heterostructure, the separation efficiency of electron-hole pairs of Ag_3PO_4 was significantly improved so that $\text{Ag}_3\text{PO}_4/\text{TiO}_2@\text{MoS}_2$ (3.5 wt%) presented higher photocatalytic activity. More than 92% Methyl orange and Methylene blue were photodegraded over $\text{Ag}_3\text{PO}_4/\text{TiO}_2@\text{MoS}_2$ (3.5 wt%) in 12 min and 5 min, respectively. More importantly, $\text{TiO}_2@\text{MoS}_2$ could play the role of 'wire' to guide electrons captured by MoS_2 and quickly transferred electrons into solution so that the recombination of electron-hole pairs and the reduction of silver irons were effectively restrained. Thus, $\text{Ag}_3\text{PO}_4/\text{TiO}_2@\text{MoS}_2$ (3.5 wt%) exhibited excellent anti-photocorrosion performance. Even after 10 cycling runs, $\text{Ag}_3\text{PO}_4/\text{TiO}_2@\text{MoS}_2$ (3.5 wt%) could degrade 75% and 92% of oxytetracycline and enrofloxacin, respectively, whereas Ag_3PO_4 degraded 23% and 44%. In addition, the possible photodegradation pathways of oxytetracycline and enrofloxacin were proposed, demonstrating that the photodegradation mechanisms involving oxidizing/shedding of functional groups firstly and opening the ring sequentially. Further detection of reactive oxidative species indicated that holes were the main active oxidizing species involved in the photocatalytic reaction process. Thus, $\text{Ag}_3\text{PO}_4/\text{TiO}_2@\text{MoS}_2$ (3.5 wt%) is a promising photocatalyst for photodegradation of organic pollutants in the environmental protection.

© 2016 Elsevier B.V. All rights reserved.

1. Introduction

In recent years, photocatalytic oxidation technology have attracted considerable attention due to its energy saving, environmental friendly performance and no secondary pollution [1,2]. Silver-containing compounds, including AgX ($X = \text{Cl}, \text{Br}, \text{I}$), Ag_3CO_3 , Ag_3PO_4 , $\text{Ag}@\text{AgX}$ ($X = \text{Cl}, \text{Br}, \text{I}$) are investigated as efficient visible light response photocatalysts for degradation of organic pollutants [3]. Among them, Ag_3PO_4 are considered to have the highest quantum efficiency of 90% at the wavelengths longer than 420 nm [4]. Yang et al. [5] synthesized the highly uniform Ag_3PO_4 microspheres with novel 3D flower-like morphology using the polyethylene glycol (PEG) as the medium, providing nucleation sites for the growth of nanosheets due to the strong interactions between activated oxygen in PEG and Ag^+ irons. The prepared 3D flower-like Ag_3PO_4 spheres exhibit excellent photocatalytic activity under visible-light

irradiation due to the larger surface area and easier separation of electron-hole pairs. Hua et al. [6] synthesized the porous Ag_3PO_4 microtubes using polyethylene glycol 200 (PEG200) as the reaction medium. Since the hydrophilic $\text{CH}_2-\text{CH}_2-\text{O}$ in PEG200 can easily form a chain-like structure, Ag^+ could combine with it and form 'Ag-PEG' which could restrict Ag^+ in ordered sequence. Dong et al. [7] synthesized Ag_3PO_4 with various morphologies (branch, tetrapod, nanorod, triangular prism) using the mixture of *N,N*-dimethylformamide (DMF) and H_2O as the reaction solvent by simply adjusting the external experimental conditions such as static or ultrasonic. However, Ag_3PO_4 was easily photo-corroded by the photogenerated electrons ($4\text{Ag}_3\text{PO}_4 + 6\text{H}_2\text{O} + 12\text{h}^+ + 12e^- \rightarrow 12\text{Ag} + 4\text{H}_3\text{PO}_4 + 3\text{O}_2$) and decomposed into the silver with low activity during the photocatalytic reactions [8]. In addition, Ag_3PO_4 photocatalyst possesses a relatively higher K_{sp} of 1.6×10^{-16} compared with other photocatalysts such as CdS ($K_{\text{sp}} 8.0 \times 10^{-27}$) and Cu_2S ($K_{\text{sp}} 2.5 \times 10^{-48}$), so Ag_3PO_4 photocatalyst could slightly dissolve as Ag^+ and PO_4^{3-} in aqueous solution [9]. These problems greatly limited the wide application of Ag_3PO_4 in photocatalytic degradation of organic pollutants.

* Corresponding author.

E-mail address: wjnnju@163.com (J. Wang).

In order to improve the photocatalytic performance, Ag_3PO_4 modification with other matching semiconductors and carbon materials including $\text{Ag}_3\text{PO}_4/\text{graphene}$ [10–12], $\text{Ag}_3\text{PO}_4/\text{BiVO}_4$ [13], $\text{Ag}_3\text{PO}_4/\text{Ag}/\text{WO}_{3-x}$ [14], $\text{Ag}_3\text{PO}_4/\text{g-C}_3\text{N}_4$ [15] had been investigated. Photocatalytic activity of these Ag_3PO_4 -based photocatalysts was enhanced by reducing the recombination of electron-hole pairs and higher visible-light absorption properties. However, most of researches focused on the improvement of photocatalytic activity, and anti-photocorrosion was not regarded as an important index to evaluate the photocatalytic performance of photocatalysts. Moreover, these layer materials which provided smaller point contact between the bulk phases usually leaded to low conjunction of Ag_3PO_4 , such as graphene, graphene oxide and $\text{g-C}_3\text{N}_4$. The lower conjunction could significantly limit the photo-induced charge separation [16]. Meanwhile, the oxidation and reunion of graphene could weaken the electronic conductivity for charge separation of the photogenerated carriers. Thus, it is essential to increase the specific surface area and contact sites of modified materials while improving the anti-photocorrosion ability of Ag_3PO_4 .

Nowadays, with the research of graphene-based materials, few-layer 2D transition metal disulfide materials have aroused people's significant attention due to their lamellar structure and excellent electron-transporting. Especially, few-layer MoS_2 with a similar lamellar structure to that of graphene, can be used in many fields, such as optoelectronics and energy harvesting, because it has a sizable bandgap and is naturally abundant [17,18]. Liu et al. [19] reported that high photoelectrochemical activity for H_2 evolution was obtained by the deposition of CdS on the surface of MoS_2 to form a *p-n* heterojunction. Shen et al. [20] prepared a kind of MoS_2 nanosheet/ TiO_2 nanowire hybrid nanostructure, which exhibited high activity in the visible light photocatalytic hydrogen evolution reaction. Moreover, several MoS_2 based photocatalysts including $\text{MoS}_2/\text{BiOBr}$ [21], $\text{MoS}_2/\text{SnO}_2$ [22] and $\text{MoS}_2/\text{Bi}_2\text{MoO}_6$ [23] were also investigated for photodegradation of organic pollutants under visible light irradiation. In addition, due to high stability and environmentally friendly nature, TiO_2 is another preferable photocatalyst for scientific research, which also attracts high attention to construct different morphology of heterostructure with Ag_3PO_4 [24,25].

Based on the research background mentioned above, novel three-dimensional (3D) hierarchical semiconductor composites $\text{Ag}_3\text{PO}_4/\text{TiO}_2@\text{MoS}_2$ were successfully synthesized in the present work. According to the excellent conductivity of MoS_2 and stability of TiO_2 , it is expected to construct $\text{Ag}_3\text{PO}_4/\text{TiO}_2@\text{MoS}_2$ with synergistic effects to improve the visible-light photocatalytic activity and anti-photocorrosion ability effectively. Notably, this novel 3D photocatalyst was much different from traditional MoS_2 modification with Ag_3PO_4 from the view of construction reported in previous literatures [3,26]. Since it was more conductive to accelerate separation of electron-hole pairs through vertical few-layer MoS_2 , $\text{Ag}_3\text{PO}_4/\text{TiO}_2@\text{MoS}_2$ showed excellent photocatalytic activity and anti-photocorrosion. Our study focused on the following three aspects: 1) to test its photocatalytic activity by degradation of Methyl orange (MO) and Methylene blue (MB), 2) to evaluate the photocatalytic stability and anti-photocorrosion of $\text{Ag}_3\text{PO}_4/\text{TiO}_2@\text{MoS}_2$ by degradation of oxytetracycline (OTC) and enrofloxacin (ENR), and 3) to propose the possible photocatalytic degradation pathways and mechanisms.

2. Experimental

2.1. Chemicals

All the chemicals were analytical grade which were purchased from Aladdin Industrial Corporation (shanghai, China).

2.2. Synthesize of $\text{Ag}_3\text{PO}_4/\text{TiO}_2@\text{MoS}_2$

2.2.1. Synthesis of Ag_3PO_4

3.40 g AgNO_3 was dissolved in 100 ml deionized water in a beaker at 60 °C. Then, an aqueous solution of Na_3PO_4 (50 ml $\text{Na}_3\text{PO}_4 \cdot 12\text{H}_2\text{O}$, 2.2807 g) was added drop wise to the breaker, and the color of the solution changed gradually from colorless to yellow. The precipitant was obtained after centrifugation, and then washed by deionized water and anhydrous ethanol. Finally, the products of Ag_3PO_4 were dried under 55 °C for 6 h.

2.2.2. Electrospinning of TiO_2 nanofibers

Typically, 0.5036 g polyvinyl pyrrolidone (PVP, 6 wt%) was dissolved in 10 ml of ethanol. Then, 2 ml isopropyl titanate and 3 ml glacial acetic acid were added in the above solution. In order to ensure the stability of the solution and avoid the emergence of the stratification, 3 ml DMF was also added into the solution. Then the solution was magnetic stirred for 3 h at 25 °C, following milky-white gradually to yellowish. Next, the mixing solution was injected into 10 ml syringe for electrostatic spinning. Electrostatic spinning parameters are as follows: electrical potential = 13 kV, flow rate = 0.5 ml/h, receiving distance = 15 cm, needle diameter = 0.8 mm, relative air humidity = 50%. All these operations were conducted at room temperature (30 °C). The as-collected nanofibers were calcined at 450 °C for 2 h in air atmosphere to remove PVP with the formation of TiO_2 crystals. PVP is used as pore-foaming agents. The porous TiO_2 nanofibers were formed in the calcination process after PVP removal.

2.2.3. Synthesize of $\text{TiO}_2@\text{MoS}_2$ heterostructure

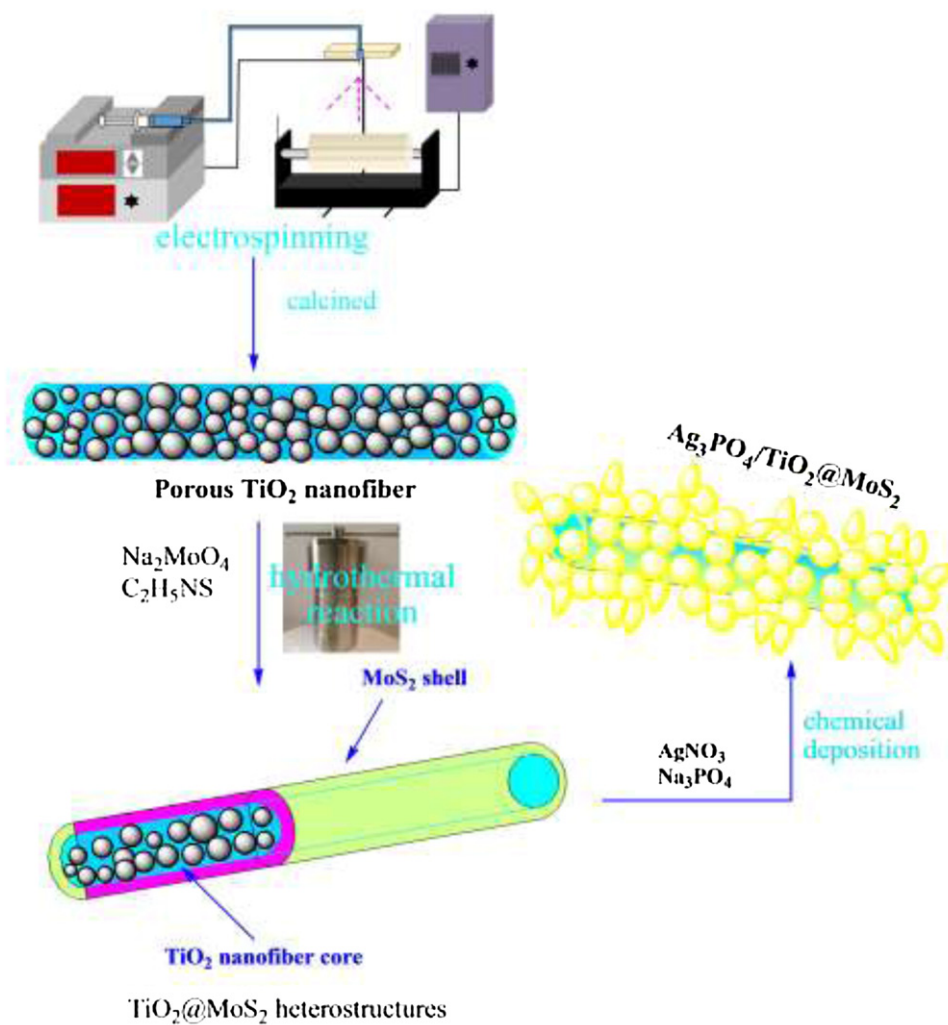
0.45 g $\text{Na}_2\text{MoO}_4 \cdot 9\text{H}_2\text{O}$ and 0.90 g $\text{C}_2\text{H}_5\text{NS}$ were dissolved in 200 ml deionized water as a transition state solution. Then 0.20 g TiO_2 nanofibers were added into the above solution, and the mixture was ultrasound for 30 min to get the suspension. The suspension was transferred to a Teflon-lined stainless steel autoclave and then heated in a high temperature oven at 220 °C for 24 h. The solid product was dried at 80 °C for 12 h to obtain $\text{TiO}_2@\text{MoS}_2$ heterostructure. In addition, the synthesis process of pure MoS_2 was similar to $\text{TiO}_2@\text{MoS}_2$ mentioned above except that TiO_2 nanofibers were not added in.

2.2.4. Synthesize of $\text{Ag}_3\text{PO}_4/\text{TiO}_2@\text{MoS}_2$

3.40 g AgNO_3 was dissolved in 100 ml deionized water in a beaker at 60 °C, adding certain amount of $\text{TiO}_2@\text{MoS}_2$ (in this paper, in the preparation process of $\text{Ag}_3\text{PO}_4/\text{TiO}_2@\text{MoS}_2$ nanomaterials, $\text{TiO}_2@\text{MoS}_2$ mass fraction were 1%, 2.5%, 3.5%, 5% and 8%). Then, an aqueous solution of Na_3PO_4 (50 ml $\text{Na}_3\text{PO}_4 \cdot 9\text{H}_2\text{O}$, 2.2807 g) was added dropwise to the breaker, and the color of solution gradually from black to yellow. The chemical deposition time is for 30 min. The products were collected after centrifugation, washed several times respectively with deionized water and anhydrous ethanol. Finally, the products obtained were dried at 55 °C for 6 h. In addition, the synthesis process of $\text{Ag}_3\text{PO}_4/\text{TiO}_2$ (3.5 wt%) and $\text{Ag}_3\text{PO}_4/\text{MoS}_2$ (3.5 wt%) composites were similar to the synthesis process of Ag_3PO_4 mentioned above except that certain proportion of MoS_2 and TiO_2 nanofibers were added into AgNO_3 solution, respectively. The synthesized process is shown in Scheme 1.

2.3. Characterization of $\text{Ag}_3\text{PO}_4/\text{TiO}_2@\text{MoS}_2$

The morphologies and microstructures of the samples were characterized using the field emission scanning electron microscope (FESEM, S-3400NII, Hitachi, Japan) and transmission electron microscope (TEM, JEOLJEM-200CX, JEOL, Japan). The EDS mapping images were captured on the atomic resolution analytical microscope (Tecnai G2 F20 S-TWIN, FEI, America). The crystal



Scheme 1. Schematic of synthesize of $\text{Ag}_3\text{PO}_4/\text{TiO}_2@\text{MoS}_2$.

phases of samples were collected on the X-ray diffractometer with Cu- ka radiation (XRD, X'TRA, Switzerland). The XRD patterns were scanned in the range of 10–80° (θ) at a scanning rate of 5° min⁻¹. The binding energies of Ag, P, Ti, Mo and S of $\text{Ag}_3\text{PO}_4/\text{TiO}_2@\text{MoS}_2$ were determined by X-ray photoelectron spectroscopy (XPS, PHI 5000 VersaProbe, UIVAC-PHI, Japan) with an Al- ka X-ray source. The photocurrent responses were determined by the electrochemical analyzer (CHI660E, Shanghai, China) with a standard three-electrode configuration, which employed a Pt wire as a counter electrode, a saturated calomel electrode as a reference electrode and fluorine-doped tin oxide (FTO) as a working electrode. The UV-vis diffuse reflectance spectra (DRS) were performed on the UV-vis spectrophotometer (UV-3600, Shimadzu, Japan) with an intergrating sphere.

2.4. Photocatalytic activity tests

Photocatalytic activities of $\text{Ag}_3\text{PO}_4/\text{TiO}_2@\text{MoS}_2$ were tested by photocatalytic degradation of methyl orange (MO) and methylene blue (MB) at 25 °C. In order to study on the influence of $\text{TiO}_2@\text{MoS}_2$ contents on photocatalytic degradation activity, $\text{Ag}_3\text{PO}_4/\text{TiO}_2@\text{MoS}_2$ with various $\text{TiO}_2@\text{MoS}_2$ contents (1.0–8.0 wt%) were used to make comparison experiment. Furthermore, in order to objectively evaluate the photocatalytic activity of 3D $\text{Ag}_3\text{PO}_4/\text{TiO}_2@\text{MoS}_2$, photocatalysts including Ag_3PO_4 , $\text{Ag}_3\text{PO}_4/\text{TiO}_2$ and $\text{Ag}_3\text{PO}_4/\text{MoS}_2$ were used to make a compara-

tive experiment. Typically, 0.25 g photocatalyst was added into MO aqueous solution (2.5 mg/L, 500 ml) in XPA-Photochemical Reactor (Xujiang Electromech-anical Plant, Nanjing, China) with a 800 w xenon (Xe) arc lamp irradiation. All photodegradation solutions were stirred in the dark for 30 min to obtain good dispersion and reach adsorption equilibrium between the substances and the surface of catalysts in this paper. During the photodegradation experiment, 5 ml suspensions were sampled at a given time interval, followed by centrifugation at 3000 rpm to separate the photocatalyst. The concentration of MO was determined by the UV-vis spectrophotometer (wavelength = 464 nm). The photocatalytic degradation rate (E%) was calculated according to Eq. (1).

$$E\% = (C_0 - C)/C_0 \times 100\% \quad (1)$$

where C_0 (mg/L) is the initial concentration, while C (mg/L) is the concentration of MO after irradiation at any time. C can be calculated through the corresponding absorbance according to the standard curve.

In addition, the multi-batches photocatalytic degradation of MB (2.5 mg/L) over Ag_3PO_4 and $\text{Ag}_3\text{PO}_4/\text{TiO}_2@\text{MoS}_2$ were performed under the same reaction conditions as those mentioned above, respectively. Typically, 0.25 g photocatalyst was added into MB aqueous solution. After sampling and centrifugation, the small amount of precipitation of photocatalyst was recirculated to reactor in order to assume the total amount of photocatalyst unchanged

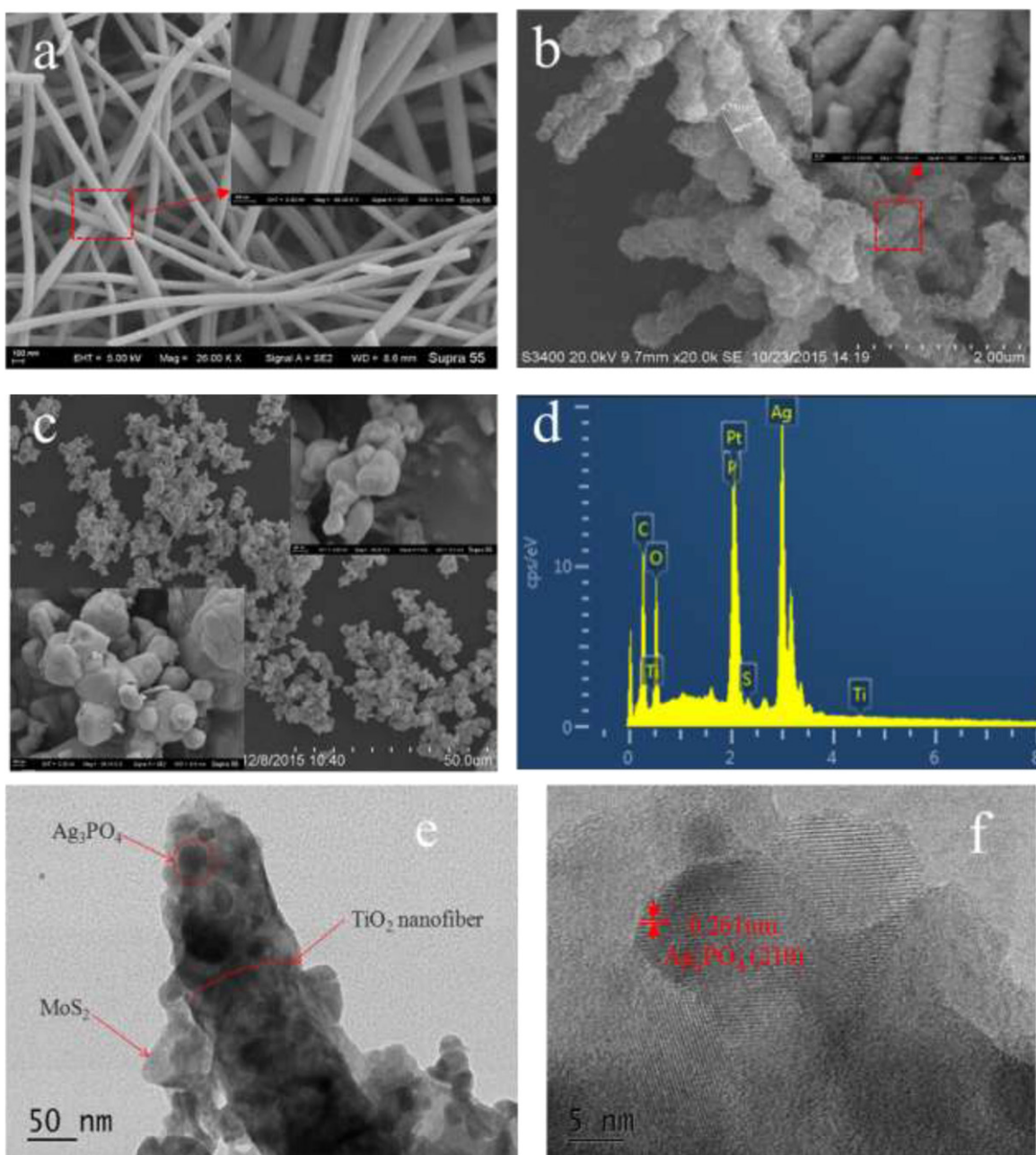


Fig. 1. SEM and FE-SEM image of (a) TiO_2 nanofibers, (b) $\text{TiO}_2@\text{MoS}_2$ heterostructure, (c) 3D hierarchical $\text{Ag}_3\text{PO}_4/\text{TiO}_2@\text{MoS}_2$ (3.5 wt%) composite, (d) EDS of $\text{Ag}_3\text{PO}_4/\text{TiO}_2@\text{MoS}_2$ (3.5 wt%) composite, (e) TEM image of $\text{Ag}_3\text{PO}_4/\text{TiO}_2@\text{MoS}_2$ (3.5 wt%), and (f) High-resolution of $\text{Ag}_3\text{PO}_4/\text{TiO}_2@\text{MoS}_2$ (3.5 wt%).

as the next batch photodegradation of MB proceeded. The detection wavelength for MB was 664 nm.

2.5. Anti-photocorrosion evaluation

In order to evaluate the anti-photocorrosion of $\text{Ag}_3\text{PO}_4/\text{TiO}_2@\text{MoS}_2$, 10 runs of photocatalytic degradations of antibiotics OTC and ENR were conducted as follows: In XPA-Photochemical Reactor (Xujiang Electromechanical Plant, Nanjing, China) with a 800 w xenon (Xe) arc lamp irradiation. 0.500 g $\text{Ag}_3\text{PO}_4/\text{TiO}_2@\text{MoS}_2$ was added into 500 ml of OTC solution (5 mg/L) and ENR solution (5 mg/L) at 25 °C, respectively. During the process of anti-photocorrosion test, 5 ml suspensions were sampled at a given time interval, followed by centrifugation at 3000 rpm to separate the photocatalyst. Then the concentration of OTC and ENR were analyzed by high performance liquid chromatography (HPLC, Agilent, America) in the process of reaction. The operating conditions for HPLC are listed in Table 1.

2.6. Photocatalytic degradation mechanism of OTC and ENR

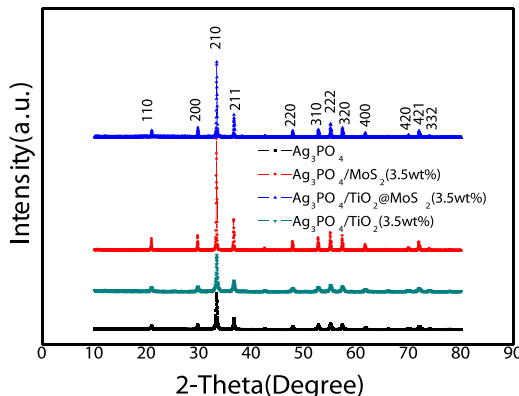
The photocatalyst degradation intermediate products of OTC and ENR were detected by high performance liquid chromatography coupled with time-of-flight mass spectrometry detection (HPLC-TOFMS, Agilent 1290 Infinity LC/6460 QQQ MS) in positive polarity.

Furthermore, the tapping experiments were conducted to determine the main reactive oxidative species. The active species generated in the photocatalytic system could be measured through trapping by ethylenediamine tetraacetic acid disodium salt (EDTA-2Na, 5 mM) and *tert*-butanol (tBuOH, 5 mM) tests. The EDTA-2Na and tBuOH were respectively added into OTC (5 mg/L) and ENR

Table 1

Operating conditions for HPLC about OTC and ENR.

| | OTC | ENR |
|------------------------|--|---|
| Mobile phase | A [Ultrapure water/methanol/H ₃ PO ₄ (85 wt%) = 500/25/2]; B (acetonitrile) | C [Tetrabutyl ammonium bromide (0.015 M, H ₃ PO ₄ adjust pH = 3.0)]; D (acetonitrile) |
| chromatographic column | Mobile phase of mixture (A/B = 7/3) 4.6 × 250 mm, 5 μm | Mobile phase of mixture (C/D = 9/1) 4.6 × 250 mm, 5 μm |
| Flow rate | 1.0 ml/min | 1.0 ml/min |
| Detector temperature | 303 K | 309 K |
| Detection wavelength | λ = 354 nm | λ = 278 nm |

**Fig. 2.** XRD patterns of Ag₃PO₄, Ag₃PO₄/TiO₂, Ag₃PO₄/MoS₂ and Ag₃PO₄/TiO₂@MoS₂ composites.

(5 mg/L) solution before photodegradation process. The reaction and operation condition was as same as Section 2.5.

3. Results and discussion

3.1. Characterization of Ag₃PO₄/TiO₂@MoS₂

3.1.1. SEM and TEM analysis

SEM and FE-SEM image could well describe the morphology of product during various synthetic processes. By using electro-spinning method, TiO₂ nanofibers is prepared with the average diameter about 180 nm (Fig. 1a). After hydrothermal reaction TiO₂@MoS₂ with 2D structure is obtained (Fig. 1b). Few-layer MoS₂ are vertical implanted onto TiO₂ fibers because O and Mo atoms can form 'Ti-O-Mo' bonds in combination with each other [27]. As a result, MoS₂ was well coated on the surface of TiO₂ fibers. Furthermore, it is observed that the vertical MoS₂ embryos grow larger into staggered MoS₂ sheets, expanding the diameter of the bare TiO₂ nanofiber from 180 nm to 420 nm of the coaxial TiO₂@MoS₂ heterostructure nanofiber. In the process of chemical deposition, Ag₃PO₄ deposited on the surface of TiO₂@MoS₂ nanofibers, and 3D morphology of composite nanomaterials Ag₃PO₄/TiO₂@MoS₂ is observed obviously (Fig. 1c). In addition, the energy dispersive X-ray spectrometry (EDX) analysis also confirms the existence of Ag, O, Ti, S and Mo in 3D Ag₃PO₄/TiO₂@MoS₂ composite (Fig. 1d).

TEM and High-resolution transmission electron microscopy (HRTEM) images can show the crystal structure of Ag₃PO₄/TiO₂@MoS₂ more intuitive (Fig. 1e, f). The few-layer MoS₂ is well coated on the surface of TiO₂ nanofiber, and large amounts of Ag₃PO₄ particles deposit on the surface of MoS₂ (Fig. 1e). Furthermore, the space of lattice fringes (Fig. 1f) of 0.261 nm of Ag₃PO₄/TiO₂@MoS₂ are corresponding to the (210) plane of Ag₃PO₄ (JCPDS 06-0505).

3.1.2. X-ray diffraction (XRD)

XRD spectra can provide more useful information of the crystal structure of the samples (Fig. 2). In the XRD pattern of Ag₃PO₄,

all of the diffraction peaks could be clearly assigned to the cubic phase of Ag₃PO₄ (JCPDS card no.06-0505). The diffraction peaks at 21.7°, 29.7°, 33.3°, 36.5°, 42.49°, 47.8°, 52.6°, 54.9°, 57.2°, 61.8° and 71.8° are respectively ascribed to the (110), (200), (210), (211), (220), (310), (222), (320), (321), (400) and (421) diffraction planes of Ag₃PO₄ [26]. Although the characteristic peaks of Ag₃PO₄ could be well observed in Ag₃PO₄/TiO₂ (3.5 wt%), Ag₃PO₄/MoS₂ (3.5 wt%) and Ag₃PO₄/TiO₂@MoS₂ (3.5 wt%) composites, there are no appearance of the corresponding characteristic peaks of TiO₂ and MoS₂ in XRD patterns due to their lower content. Moreover, TiO₂@MoS₂ in Ag₃PO₄/TiO₂@MoS₂ (3.5 wt%) composite did not obviously change the characteristic peak positions of Ag₃PO₄, suggesting that TiO₂@MoS₂ was not incorporated into the Ag₃PO₄ lattice.

3.1.3. X-ray photoelectron spectroscopy (XPS)

In the present work, XPS is used to further analyze the elemental compositions of the prepared samples. The full scanned XPS spectra of Ag₃PO₄/TiO₂@MoS₂ (3.5 wt%) demonstrates the existing of elements of Ag, P, Ti, Mo and S, which is consistent with the result of EDX analysis (Fig. 3a). As discerned from the XPS spectra of Ag 3d (Fig. 3b), there are two individual peaks at 366.2 eV and 372.8 eV, which can be attributed to 3d3/2 and 3d5/2 of typical Ag⁺, respectively [24,28–31]. The characteristic peak (P 2p) of at 132.5 eV (Fig. 3c) corresponds to P⁵⁺ according to the previous literatures [24,28–30]. The Ti 2p binding energy peaks (Fig. 3d) of 457.2 eV and 465.4 eV suggest the existence of Ti⁴⁺ in the composite [28,29,32,33]. Furthermore, the Mo 3d XPS spectra (Fig. 3e) shows binding energy of 231.3 eV for Mo⁴⁺ 3d5/2 and 234.5 eV for Mo⁴⁺ 3d3/2, suggesting that Mo is in oxidation state (+4) [3,26]. In addition, characteristic peaks of S 2p (Fig. 3f) at 160.8 eV and 162.7 eV belong to S 2p2/3 and S 2p1/2, respectively, indicating that S is in reduction state (-2) [3,26]. Thus, the XPS spectra of Ag₃PO₄/TiO₂@MoS₂ confirmed that preparation method of photocatalyst is feasible.

3.1.4. Photocurrent test

The photocurrent of photocatalysts can be used to evaluate the ability of producing charge carriers and the separation of photogenerated electrons. The mass fraction of TiO₂@MoS₂ in Ag₃PO₄/TiO₂@MoS₂ composite shows nonlinear influence on photocatalytic degradation activity (Fig. 4). Compared with Ag₃PO₄, the photocurrent intensity of Ag₃PO₄/TiO₂@MoS₂ is greatly improved and tends to be steady as TiO₂@MoS₂ content increases from 2.5 to 5 wt%. However, as TiO₂@MoS₂ content of Ag₃PO₄/TiO₂@MoS₂ increases to 8 wt%, the few-layer MoS₂ makes photocurrent drop rapidly. This was because that excess loaded of TiO₂@MoS₂ could hinder the light from contacting the Ag₃PO₄ nanoparticles and perhaps cover the practical reactive sites of Ag₃PO₄ nanoparticles.

3.1.5. UV/vis diffuse reflectance spectrum

In order to comparative study of Ag₃PO₄/TiO₂@MoS₂ (3.5 wt%) distinctive photocatalytic performance, we prepared Ag₃PO₄/TiO₂ (3.5 wt%), Ag₃PO₄/MoS₂ (3.5 wt%) to make further comparison and analysis. Generally, UV/vis diffuse reflectance spectrum was measured to characterize the optical band gap and absorption

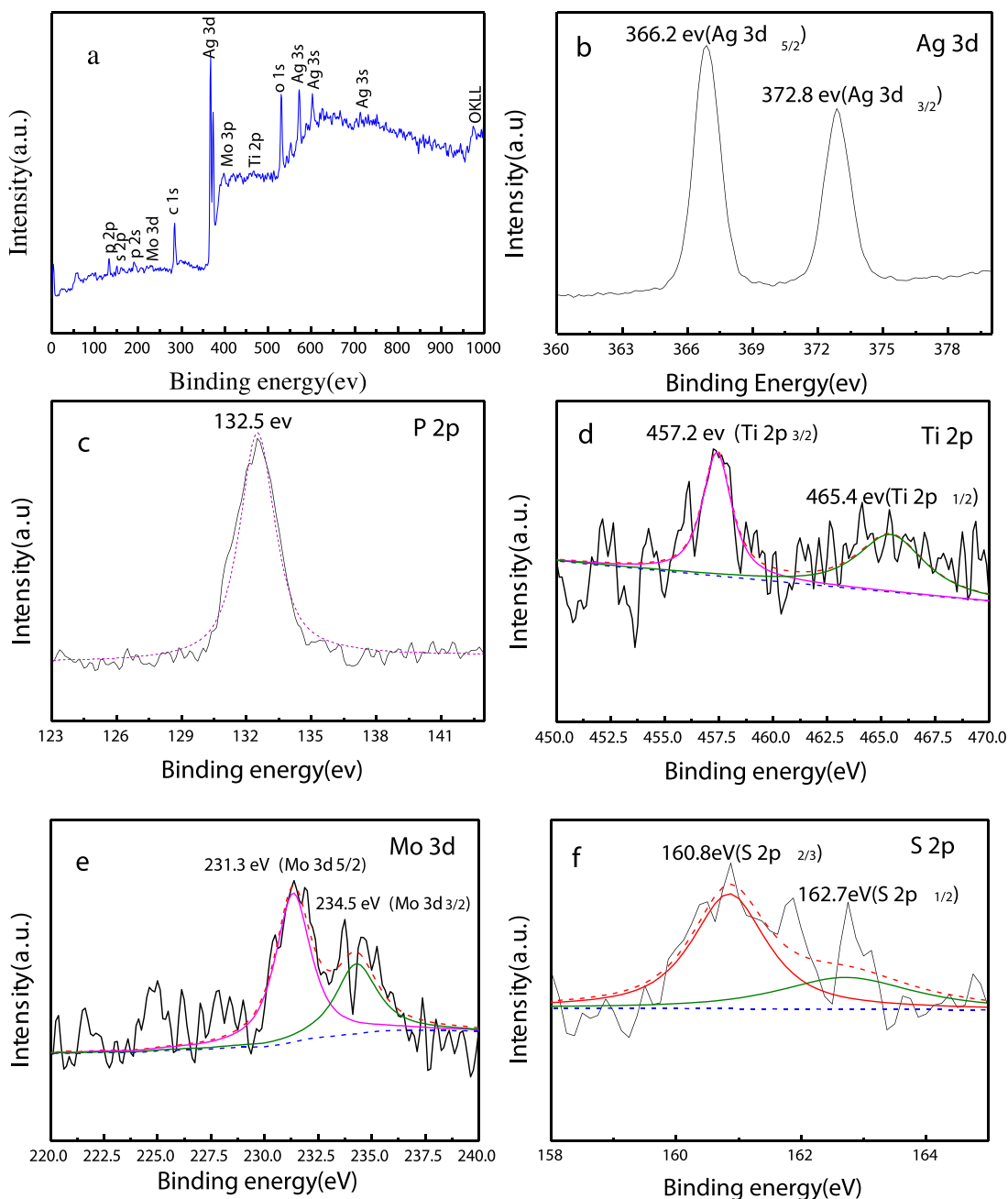


Fig. 3. XPS spectra of the $\text{Ag}_3\text{PO}_4/\text{TiO}_2@\text{MoS}_2$ (3.5 wt%) nanocomposite: (a) survey spectrum, (b) Ag 3d, (c)P 2p, (d) Ti 2p, (e) Mo 3d and (f) S 2p.

capability. The band gap of $\text{Ag}_3\text{PO}_4/\text{TiO}_2@\text{MoS}_2$ approximately is 1.85 eV (Fig. 5), far less than that of Ag_3PO_4 (2.45 eV) in previous reports [34]. Hence, compared with Ag_3PO_4 , the 3D composite $\text{Ag}_3\text{PO}_4/\text{TiO}_2@\text{MoS}_2$ (3.5 wt%) efficiently enhanced light absorption capability at the range of 200~800 nm wavelength. Meanwhile, the existing of $\text{TiO}_2@\text{MoS}_2$ also increased light absorption intensity compared with $\text{Ag}_3\text{PO}_4/\text{MoS}_2$. It can be explained as follows: $\text{TiO}_2@\text{MoS}_2$ heterostructure maximally expose edge sites of MoS_2 , reducing electrons and holes recombination rate of Ag_3PO_4 . On the other hand, $\text{TiO}_2@\text{MoS}_2$ heterostructure could avoid the face-to-face restacking of MoS_2 , resulting in better separation of photogenerated electrons. Therefore, $\text{Ag}_3\text{PO}_4/\text{TiO}_2@\text{MoS}_2$ (3.5 wt%) exhibited higher photocatalytic activity compared with $\text{Ag}_3\text{PO}_4/\text{MoS}_2$ (3.5 wt%).

3.2. Photocatalytic degradation activity tests

3.2.1. Photocatalytic degradation of MO

The photocatalytic activity can be evaluated by testing the photocatalytic degradation rate of target pollutants directly. About 90–95% of MO is photocatalytic degraded by $\text{Ag}_3\text{PO}_4/\text{TiO}_2@\text{MoS}_2$ as the mass fraction of $\text{TiO}_2@\text{MoS}_2$ ranged from 2.5 to 5 wt% (Fig. 6a). However, the photocatalytic degradation rate of MO by $\text{Ag}_3\text{PO}_4/\text{TiO}_2@\text{MoS}_2$ (8.0 wt%) dropped by 27% compared with Ag_3PO_4 . In addition, as $\text{TiO}_2@\text{MoS}_2$ content decreased to 1 wt%, few-layer MoS_2 played a small role in separation of electron-hole pairs, causing the loss of oxidation ability due to the decline of Ag_3PO_4 content. Thus, the photocatalytic activity of $\text{Ag}_3\text{PO}_4/\text{TiO}_2@\text{MoS}_2$ (1.0 wt%) was lower than that of Ag_3PO_4 . Thus, photodegradation rate of MO are in accordance to photocurrent

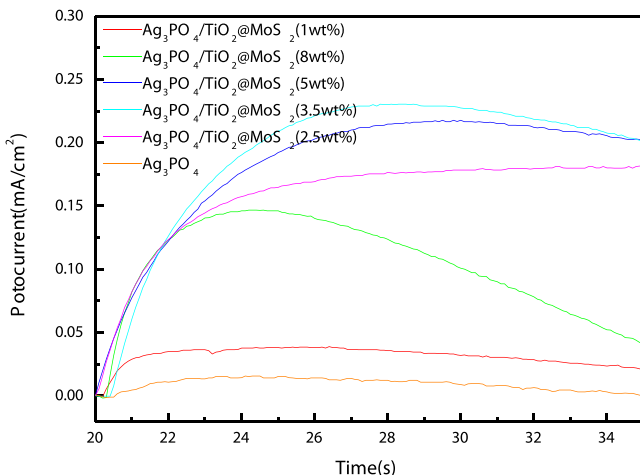


Fig. 4. Photoluminescence spectra of Ag_3PO_4 and $\text{Ag}_3\text{PO}_4/\text{TiO}_2@\text{MoS}_2$ composites.

(Fig. 4), indicating that $\text{Ag}_3\text{PO}_4/\text{TiO}_2@\text{MoS}_2$ (3.5 wt%) showed the highest photocatalytic activity in the present study.

Moreover, the photocatalytic degradation kinetic process of MO could be well described by the pseudo-first-order kinetic model ($-\ln C/C_0 = kt$) (Fig. 6b), where ' C_0 ' is the initial concentration of MO, ' C_t ' is the concentration of reactant at time ' t ', and ' k ' is the rate constant.

As listed in Table 2, $\text{Ag}_3\text{PO}_4/\text{TiO}_2@\text{MoS}_2$ (3.5 wt%) shows the highest rate constant (0.2085 min^{-1}), which was as 2.5 times as that of Ag_3PO_4 (0.0834 min^{-1}). The rate constants followed the order of $\text{Ag}_3\text{PO}_4/\text{TiO}_2@\text{MoS}_2$ (3.5 wt%)> $\text{Ag}_3\text{PO}_4/\text{TiO}_2@\text{MoS}_2$ (2.0 wt%)> $\text{Ag}_3\text{PO}_4/\text{TiO}_2@\text{MoS}_2$ (5.0 wt%)> $\text{Ag}_3\text{PO}_4/\text{TiO}_2@\text{MoS}_2$ (1.0 wt%)> $\text{Ag}_3\text{PO}_4/\text{TiO}_2@\text{MoS}_2$ (8.0 wt%), which is in accordance with the result of photocurrent in Section 3.1.4 (Fig. 4). Based on the photocatalytic activity test, $\text{Ag}_3\text{PO}_4/\text{TiO}_2@\text{MoS}_2$ (3.5 wt%) which exhibits the optical photocatalytic degradation dynamic performance was used for further study.

In addition, in order to objectively evaluate the photocatalytic activity of 3D $\text{Ag}_3\text{PO}_4/\text{TiO}_2@\text{MoS}_2$, photocatalysts reported in previous literatures including Ag_3PO_4 , $\text{Ag}_3\text{PO}_4/\text{TiO}_2$ and $\text{Ag}_3\text{PO}_4/\text{MoS}_2$

are used to make a comparative experiment (Fig. 7a). Although $\text{Ag}_3\text{PO}_4/\text{MoS}_2$ (3.5 wt%) could degrade 87.8% MO in 16 min, its degradation rate was still lower 8% than $\text{Ag}_3\text{PO}_4/\text{TiO}_2@\text{MoS}_2$ (3.5 wt%). This result was attributed to the bandgap difference of two composites (Fig. 5). Meanwhile, the photocatalytic degradation kinetic process of MO can be well described by the pseudo-first-order kinetic model (Fig. 7b). The corresponding rate constants (k) and regression coefficients (R^2) are calculated and listed in Table 3. The rate constants of $\text{Ag}_3\text{PO}_4/\text{TiO}_2@\text{MoS}_2$ (3.5 wt%) were higher than that of $\text{Ag}_3\text{PO}_4/\text{MoS}_2$ (3.5 wt%) and $\text{Ag}_3\text{PO}_4/\text{TiO}_2$ (3.5 wt%), which demonstrated better photocatalytic performance of $\text{Ag}_3\text{PO}_4/\text{TiO}_2@\text{MoS}_2$ (3.5 wt%).

3.2.2. Photocatalytic degradation of MB

Subsequently, the sequential runs of photocatalytic degradation of MB solution (2.5 mg/L) by $\text{Ag}_3\text{PO}_4/\text{TiO}_2@\text{MoS}_2$ (3.5 wt%) and Ag_3PO_4 are conducted (Fig. 8a). It was observed that the photocatalytic degradation rate of MB by Ag_3PO_4 declined significantly with the increase of recycling times. Compared with its first time use, the degradation rate of MB fell by 35% at the 6th recycling use. However, it was interesting that the photodegradation rate of MB by $\text{Ag}_3\text{PO}_4/\text{TiO}_2@\text{MoS}_2$ (3.5 wt%) could still remain more than 95% at the 6th recycle. Such improvement of anti-photocorrosion of $\text{Ag}_3\text{PO}_4/\text{TiO}_2@\text{MoS}_2$ (3.5 wt%) could be explained as follows: As Ag_3PO_4 nanoparticles were deposited on the surface of $\text{TiO}_2@\text{MoS}_2$ heterostructure, the photogenerated electrons in the conduction band of Ag_3PO_4 could be captured rapidly by few-layer MoS_2 due to high conductivity of few-layer MoS_2 . Thus, the photocorrosion of Ag_3PO_4 ($4\text{Ag}_3\text{PO}_4 + 6\text{H}_2\text{O} + 12\text{h}^+ + 12e^- \rightarrow 12\text{Ag} + 4\text{H}_3\text{PO}_4 + 3\text{O}_2$) by the photo-generated electrons were effectively inhibited, resulting in highly stable photocatalytic activity of $\text{Ag}_3\text{PO}_4/\text{TiO}_2@\text{MoS}_2$ (3.5 wt%).

The different anti-photocorrosion ability between Ag_3PO_4 and $\text{Ag}_3\text{PO}_4/\text{TiO}_2@\text{MoS}_2$ (3.5 wt%) could also be observed directly from the changes of photocatalyst color with the photodegradation proceeding. After repeating photodegradation of MB for six cycles, the color of Ag_3PO_4 changed from yellow to black (Fig. 8c), while the color of $\text{Ag}_3\text{PO}_4/\text{TiO}_2@\text{MoS}_2$ (3.5 wt%) kept unchanged (Fig. 8d). Moreover, the surface components and composition of $\text{Ag}_3\text{PO}_4/\text{TiO}_2@\text{MoS}_2$ (3.5 wt%) before and after photocatalytic reac-

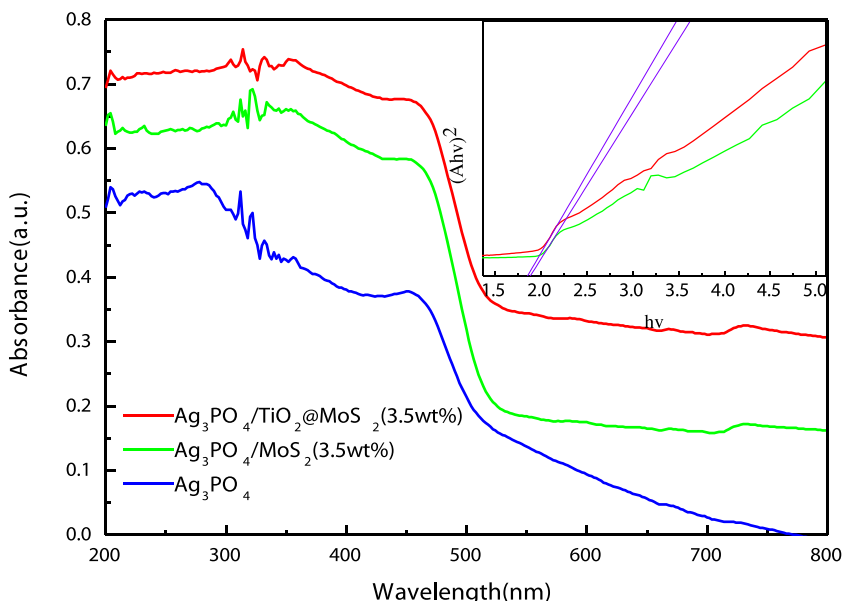


Fig. 5. UV-vis absorption spectra of Ag_3PO_4 , $\text{Ag}_3\text{PO}_4/\text{MoS}_2$ (3.5 wt%) and $\text{Ag}_3\text{PO}_4/\text{TiO}_2@\text{MoS}_2$ (3.5 wt%) composites. Inset is the corresponding kubelka-Munk transformed reflectance spectra to determine the bandgap values for the $\text{Ag}_3\text{PO}_4/\text{MoS}_2$ (3.5 wt%) and $\text{Ag}_3\text{PO}_4/\text{TiO}_2@\text{MoS}_2$ (3.5 wt%) composites.

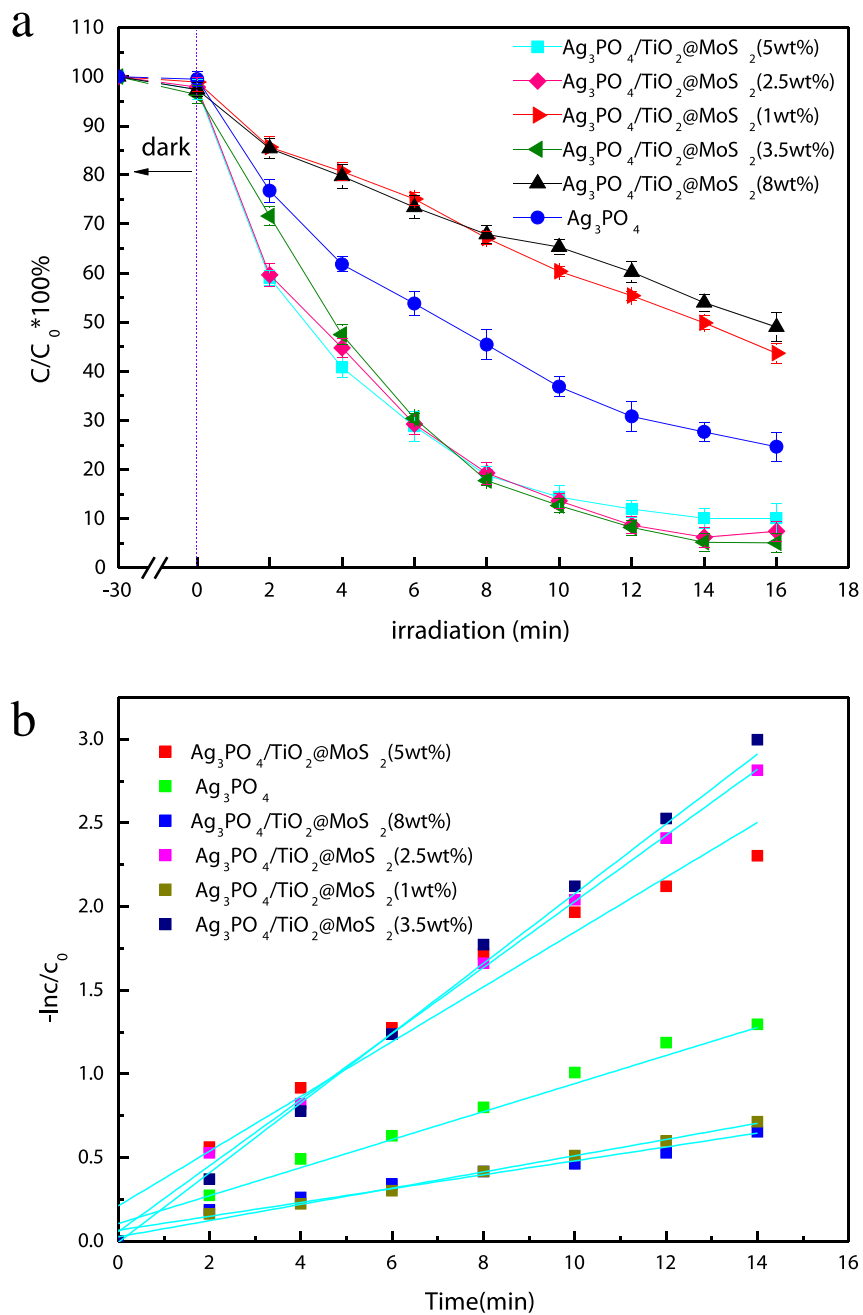


Fig. 6. (a) Photocatalytic degradation of MO solution by Ag_3PO_4 and $\text{Ag}_3\text{PO}_4/\text{TiO}_2@\text{MoS}_2$ composites, and the inset shows the color changes over time with $\text{Ag}_3\text{PO}_4/\text{TiO}_2@\text{MoS}_2$ (3.5 wt%) photocatalytic degradation, (b) Pseudo-first-order kinetic model fits the degradation kinetic curves of MO.

Table 2

The pseudo-first-order kinetic equations, rate constants (k) and regression coefficients (R^2) of photocatalytic degradation of MO over pure Ag_3PO_4 and $\text{Ag}_3\text{PO}_4/\text{TiO}_2@\text{MoS}_2$ composites.

| Series | Photocatalyst | The first order kinetic equation | $K(\text{min}^{-1})$ | R^2 |
|--------|--|----------------------------------|----------------------|-------|
| 1 | Ag_3PO_4 | $-\ln(C/C_0) = 0.0834t$ | 0.0834 | 0.930 |
| 2 | $\text{Ag}_3\text{PO}_4/\text{TiO}_2@\text{MoS}_2$ (1.0 wt%) | $-\ln(C/C_0) = 0.0485t$ | 0.0485 | 0.992 |
| 3 | $\text{Ag}_3\text{PO}_4/\text{TiO}_2@\text{MoS}_2$ (2.5 wt%) | $-\ln(C/C_0) = 0.1975t$ | 0.1975 | 0.998 |
| 4 | $\text{Ag}_3\text{PO}_4/\text{TiO}_2@\text{MoS}_2$ (3.5 wt%) | $-\ln(C/C_0) = 0.2085t$ | 0.2085 | 0.995 |
| 5 | $\text{Ag}_3\text{PO}_4/\text{TiO}_2@\text{MoS}_2$ (5.0 wt%) | $-\ln(C/C_0) = 0.1637t$ | 0.1637 | 0.963 |
| 6 | $\text{Ag}_3\text{PO}_4/\text{TiO}_2@\text{MoS}_2$ (8.0 wt%) | $-\ln(C/C_0) = 0.0415t$ | 0.0415 | 0.964 |

tion were analyzed by XPS spectra. In Fig. 8(b), peaks at 368.2 and 372.8 eV could be ascribed to the binding energies of $\text{Ag } 3d_{5/2}$ and $3d_{3/2}$ of Ag^+ (Ag_3PO_4), respectively. After the 6th runs, the $\text{Ag } 3d_{5/2}$ and $3d_{3/2}$ peaks of Ag_3PO_4 showed no obvious shift. The

result suggested that Ag^+ was not obviously reduced after sixth recycling photocatalytic reaction [16], which was in accordance with the unchanged color of $\text{Ag}_3\text{PO}_4/\text{TiO}_2@\text{MoS}_2$ (3.5 wt%) after photocatalytic degradation. In addition, it was found that the quan-

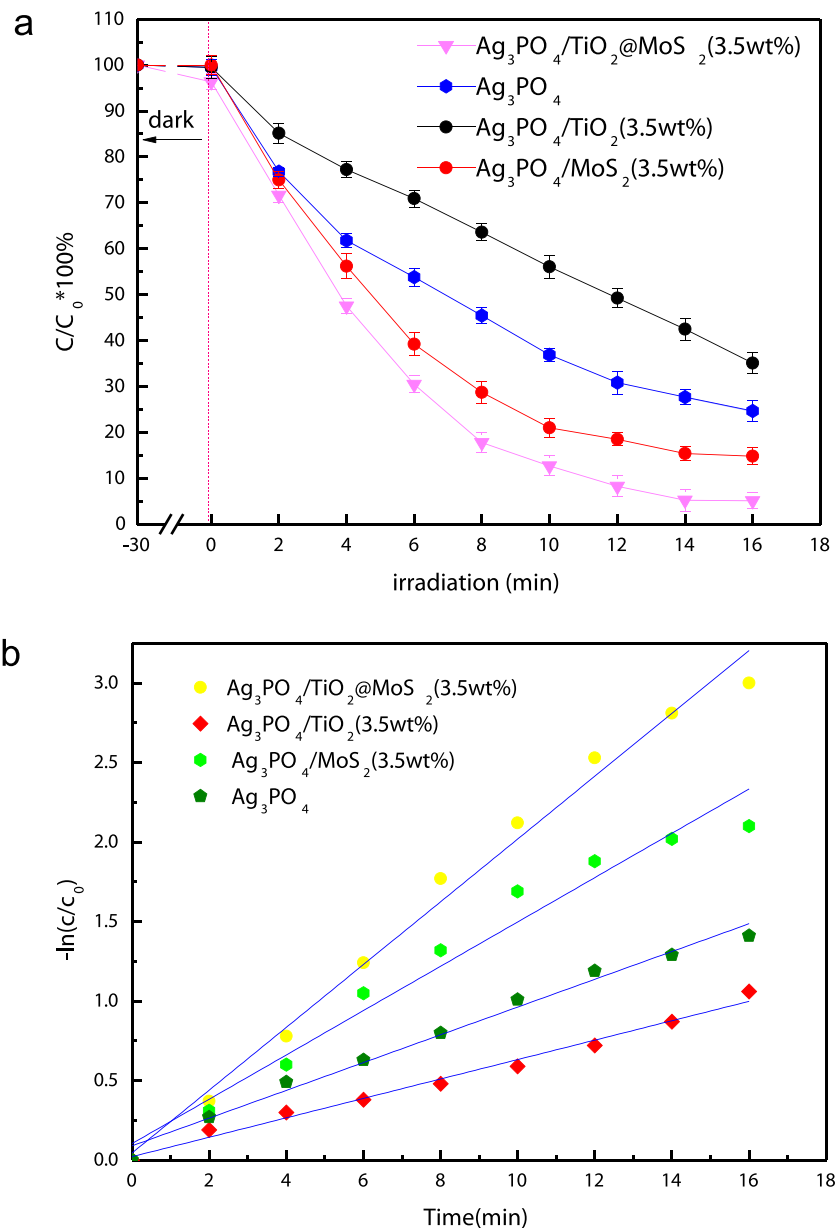


Fig. 7. (a) Photocatalytic degradation of MO by using Ag_3PO_4 , $\text{Ag}_3\text{PO}_4/\text{MoS}_2$, $\text{Ag}_3\text{PO}_4/\text{TiO}_2$ and $\text{Ag}_3\text{PO}_4/\text{TiO}_2\text{@MoS}_2$; (b) Pseudo-first-order kinetic model fits the degradation kinetic curves of MO.

Table 3
The pseudo-first-order kinetic equations, rate constant (k) and regression coefficients (R^2) of photocatalytic degradation of MO over pure Ag_3PO_4 , $\text{Ag}_3\text{PO}_4/\text{TiO}_2$, $\text{Ag}_3\text{PO}_4/\text{MoS}_2$ and $\text{Ag}_3\text{PO}_4/\text{TiO}_2\text{@MoS}_2$ composites.

| Series | Photocatalyst | The first order kinetic equation | $K(\text{min}^{-1})$ | R^2 |
|--------|--|----------------------------------|----------------------|-------|
| 1 | $\text{Ag}_3\text{PO}_4/\text{TiO}_2\text{@MoS}_2$ (3.5 wt%) | $-\ln(C/C_0) = 0.1975t$ | 0.1975 | 0.988 |
| 2 | $\text{Ag}_3\text{PO}_4/\text{TiO}_2$ (3.5 wt%) | $-\ln(C/C_0) = 0.0610t$ | 0.0610 | 0.985 |
| 3 | $\text{Ag}_3\text{PO}_4/\text{MoS}_2$ (3.5 wt%) | $-\ln(C/C_0) = 0.1394t$ | 0.1394 | 0.965 |
| 4 | Ag_3PO_4 | $-\ln(C/C_0) = 0.0873t$ | 0.0873 | 0.986 |

tivity of Ag_3PO_4 was less than that of $\text{Ag}_3\text{PO}_4/\text{TiO}_2\text{@MoS}_2$ (3.5 wt%) after 6 successive recycling uses. On one hand, the conjunction between $\text{TiO}_2\text{@MoS}_2$ with Ag_3PO_4 could decrease the dissolution of Ag_3PO_4 particles during reaction process. On the other hand, better settling ability of $\text{Ag}_3\text{PO}_4/\text{TiO}_2\text{@MoS}_2$ (3.5 wt%) could well resolve the problem of photocatalyst lost in aqueous solution. The outstanding recycling photocatalytic performance and longevity on the $\text{Ag}_3\text{PO}_4/\text{TiO}_2\text{@MoS}_2$ (3.5 wt%) make it promising candidate in practical applications.

3.3. Anti-photocorrosion evaluation

From the view of the practical application, OTC (5 mg/L) and ENR (5 mg/L) solutions were used to further evaluate the anti-photocorrosion and photocatalytic degradation stability of $\text{Ag}_3\text{PO}_4/\text{TiO}_2\text{@MoS}_2$ (3.5 wt%). The representative spectra changes of the OTC solution as a function of reaction time under irradiation show that characteristic peak is significantly reduced with the increase of the irradiation time in 24 min (Fig. 9a).

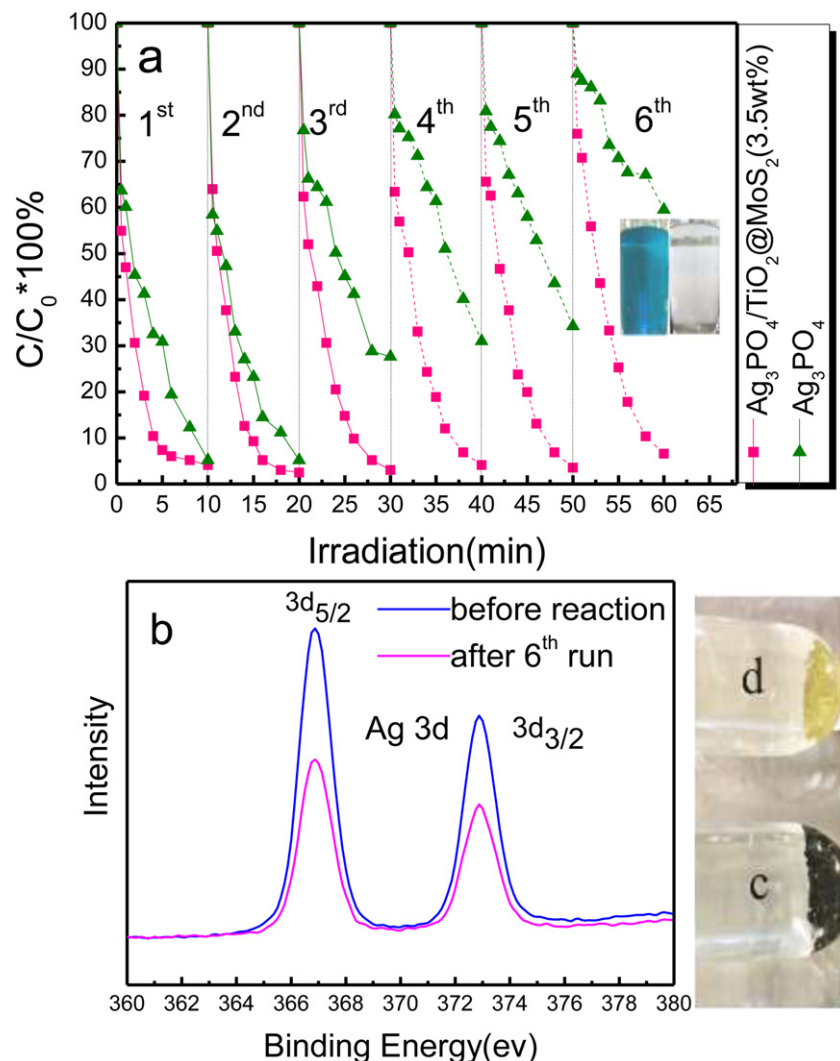


Fig. 8. (a) Cyclic performance of Ag_3PO_4 and $\text{Ag}_3\text{PO}_4/\text{TiO}_2@\text{MoS}_2$ (3.5 wt%) for the photodegradation of MB under irradiation; The color contrast of MB (left inset) after the first photodegradation by $\text{Ag}_3\text{PO}_4/\text{TiO}_2@\text{MoS}_2$ (3.5 wt%); (b) Ag 3d XPS spectra of $\text{Ag}_3\text{PO}_4/\text{TiO}_2@\text{MoS}_2$ (3.5 wt%) before and after sixth recycling photodegradation of MB; The color of photocatalyst (right inset) after 6 runs of photodegradation (c) Ag_3PO_4 (d) $\text{Ag}_3\text{PO}_4/\text{TiO}_2@\text{MoS}_2$ (3.5 wt%).

Furthermore, the recycle experiments are carried out using $\text{Ag}_3\text{PO}_4/\text{TiO}_2@\text{MoS}_2$ (3.5 wt%) composite (Fig. 9b, c), which indicates that $\text{Ag}_3\text{PO}_4/\text{TiO}_2@\text{MoS}_2$ (3.5 wt%) has high photocatalytic stability and anti-photocorrosion. After 10 successive cycling runs, the photodegradation rate of OTC still remained more than 80% within 24 min, which only declined 10% compared with that of its first time use. In addition, the photodegradation of ENR is repeated for 10 times using same photocatalyst (Fig. 9e, f). Similar to OTC, ENR could be efficiently photodegraded after 10 successive cycling runs, also demonstrating excellent anti-photocorrosion and photocatalytic stability of $\text{Ag}_3\text{PO}_4/\text{TiO}_2@\text{MoS}_2$ (3.5 wt%). Subsequently, we also analyzed the $\text{Ag}_3\text{PO}_4/\text{TiO}_2@\text{MoS}_2$ (3.5 wt%) by XPS spectra before and after recycling photodegradation of OTC and ENR (Fig. 9d, h). After the 10th runs, the $\text{Ag } 3d_{5/2}$ and $\text{Ag } 3d_{3/2}$ peaks of Ag_3PO_4 showed no obvious shift. The result imply no obvious of metallic Ag was found in the process of photocatalytic reaction.

3.4. Photocatalytic degradation pathway of OTC and ENR

The intermediate products during the photocatalytic process are identified by LC-MS/TOF, and iron spectra at different retention time (RT) of OTC photocatalytic sample before and after (1 and 8 min) are presented in ESI Scan (Supplementary material

Fig.SI-1) Typical irons spectra of OTC at RT = 8.3 min was detected in original solution. The product iron at $m/z = 461.10([\text{M} + \text{H}]^+)$ can be identified as $\text{C}_{22}\text{H}_{24}\text{N}_2\text{O}_9$. In the OTC solution after photocatalytic degradation under UV-vis irradiation, six irons spectra at RT = 4.2–14.2 min was detected. These main product irons at $m/z = 416.8([\text{M} + \text{H}]^+)$, $m/z = 402.8([\text{M} + \text{H}]^+)$, $m/z = 344.2([\text{M} + \text{H}]^+)$, $m/z = 302.2([\text{M} + \text{H}]^+)$, $m/z = 274.8([\text{M} + \text{H}]^+)$ and $m/z = 202.1([\text{M} + \text{Na}]^+)$ might be identified as $\text{C}_{21}\text{H}_{22}\text{NO}_8$, $\text{C}_{20}\text{H}_{18}\text{O}_9$, $\text{C}_{19}\text{H}_{21}\text{NO}_5$, $\text{C}_{17}\text{H}_{17}\text{O}_5$, $\text{C}_{16}\text{H}_{17}\text{O}_4$ and $\text{C}_9\text{H}_6\text{O}_4$. Based on the molecular weight and previous reports [35–45], the possible photocatalytic degradation pathways of OTC are proposed and shown in Scheme 2.

Similarly, iron spectra at different retention time (RT) of ENR photocatalytic sample before and after (1, 3 and 8 min) are presented in ESI Scan (Supplementary material Fig. SI-2). The product iron at $m/z = 360.20$ was corresponding to $\text{C}_{19}\text{H}_{12}\text{FN}_3\text{O}_3$ (ENR) in original solution. The weak spectra of product iron at $m/z = 302.20$ was ascribed to the part hydrolysis of ENR. During the photocatalytic process of ENR, nine main irons spectra at RT = 3.769–5.611 min were detected. These products irons at $m/z = 390.14([\text{M} + \text{H}]^+)$, $m/z = 362.10([\text{M} + \text{H}]^+)$, $m/z = 338.10([\text{M} + \text{H}]^+)$, $m/z = 302.20([\text{M} + \text{H}]^+)$, $m/z = 275.30([\text{M} + \text{H}]^+)$, $m/z = 242.30([\text{M} + \text{H}]^+)$, $m/z = 218.20([\text{M} + \text{H}]^+)$

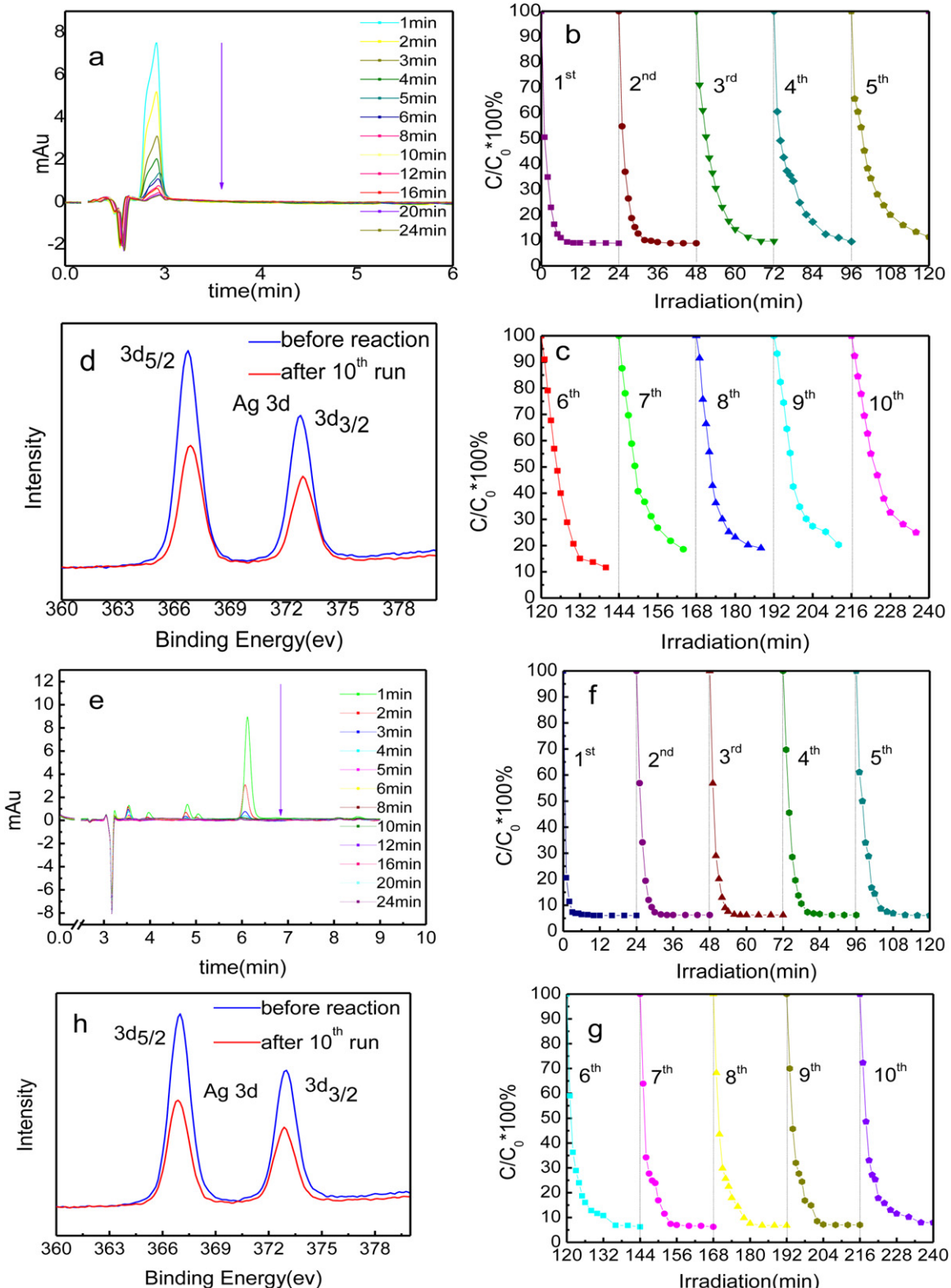
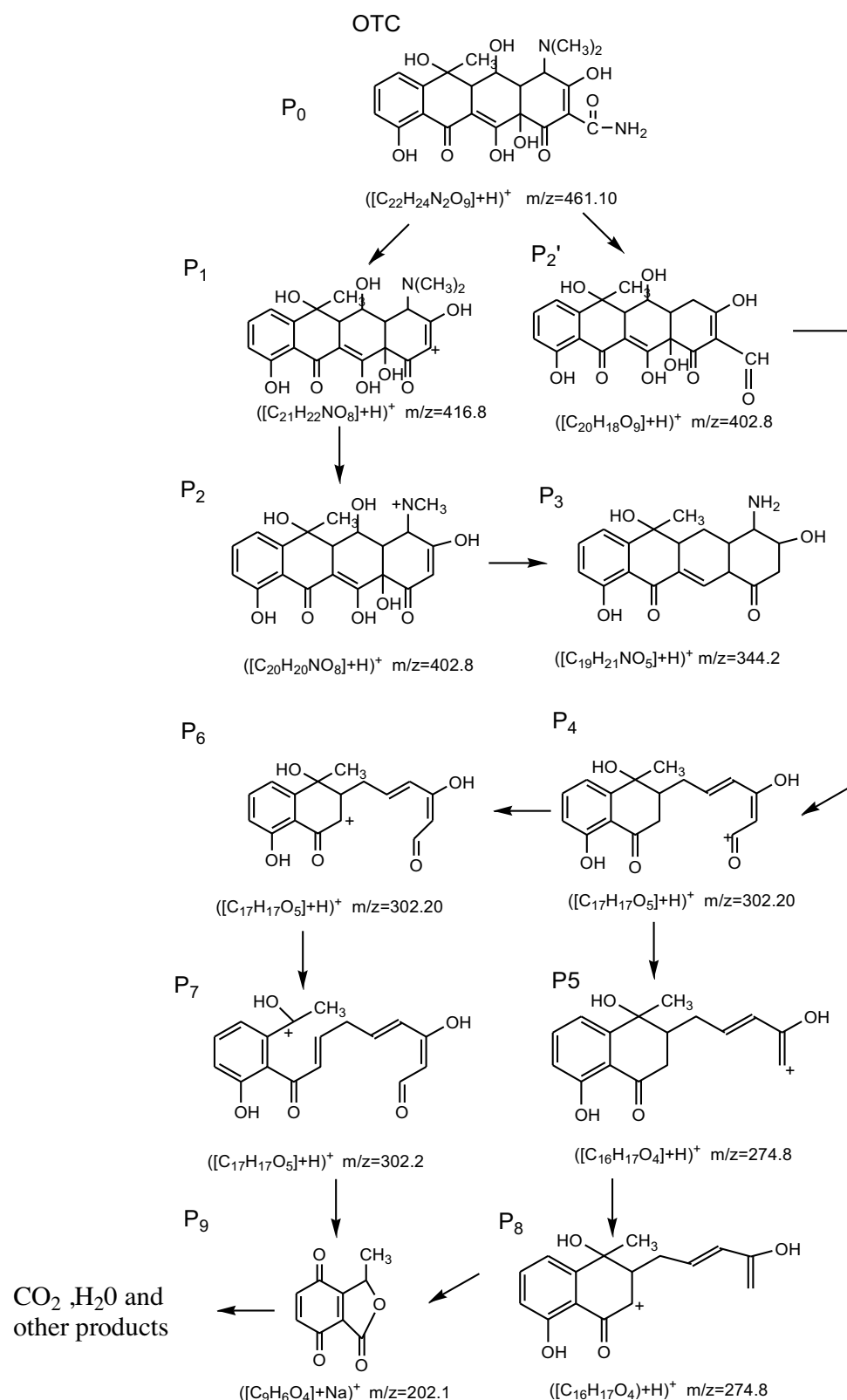


Fig. 9. (a) The liquid phase chromatogram of OTC at different reaction time; (b) and (c) cyclic performance of $\text{Ag}_3\text{PO}_4/\text{TiO}_2@\text{MoS}_2$ (3.5 wt%) for photodegradation of OTC under Xe lamp irradiation; (d) Ag 3d XPS spectra before and after recycling photodegradation of OTC by $\text{Ag}_3\text{PO}_4/\text{TiO}_2@\text{MoS}_2$ (3.5 wt%); (e) The liquid phase chromatogram of ENR at different reaction time; (f) and (g) cyclic performance of $\text{Ag}_3\text{PO}_4/\text{TiO}_2@\text{MoS}_2$ (3.5 wt%) for the photodegradation of ENR under Xe lamp irradiation; (h) Ag 3d XPS spectra before and after recycling photodegradation of ENR by $\text{Ag}_3\text{PO}_4/\text{TiO}_2@\text{MoS}_2$ (3.5 wt%).

$([\text{M} + \text{H}]^+), m/z = 202.20$ ($[\text{M} + \text{H}]^+$) and $m/z = 118.10$ ($[\text{M} + \text{H}]^+$) might be identified as $\text{C}_{19}\text{H}_{20}\text{FN}_3\text{O}_5$, $\text{C}_{17}\text{H}_{16}\text{FN}_3\text{O}_5$, $\text{C}_{19}\text{H}_{20}\text{N}_3\text{O}_3$, $\text{C}_{16}\text{H}_{19}\text{N}_3\text{O}_3$, $\text{C}_{15}\text{H}_{18}\text{N}_2\text{O}_3$, $\text{C}_{13}\text{H}_{10}\text{N}_2\text{O}_3$, $\text{C}_{10}\text{H}_6\text{N}_2\text{O}_4$, $\text{C}_{10}\text{H}_5\text{N}_2\text{O}_3$

and $\text{C}_5\text{H}_{12}\text{NO}_2$. Based on the molecular weight of the compound and previous research [46–57], the possible photodegradation pathways are proposed and shown in Scheme 3.

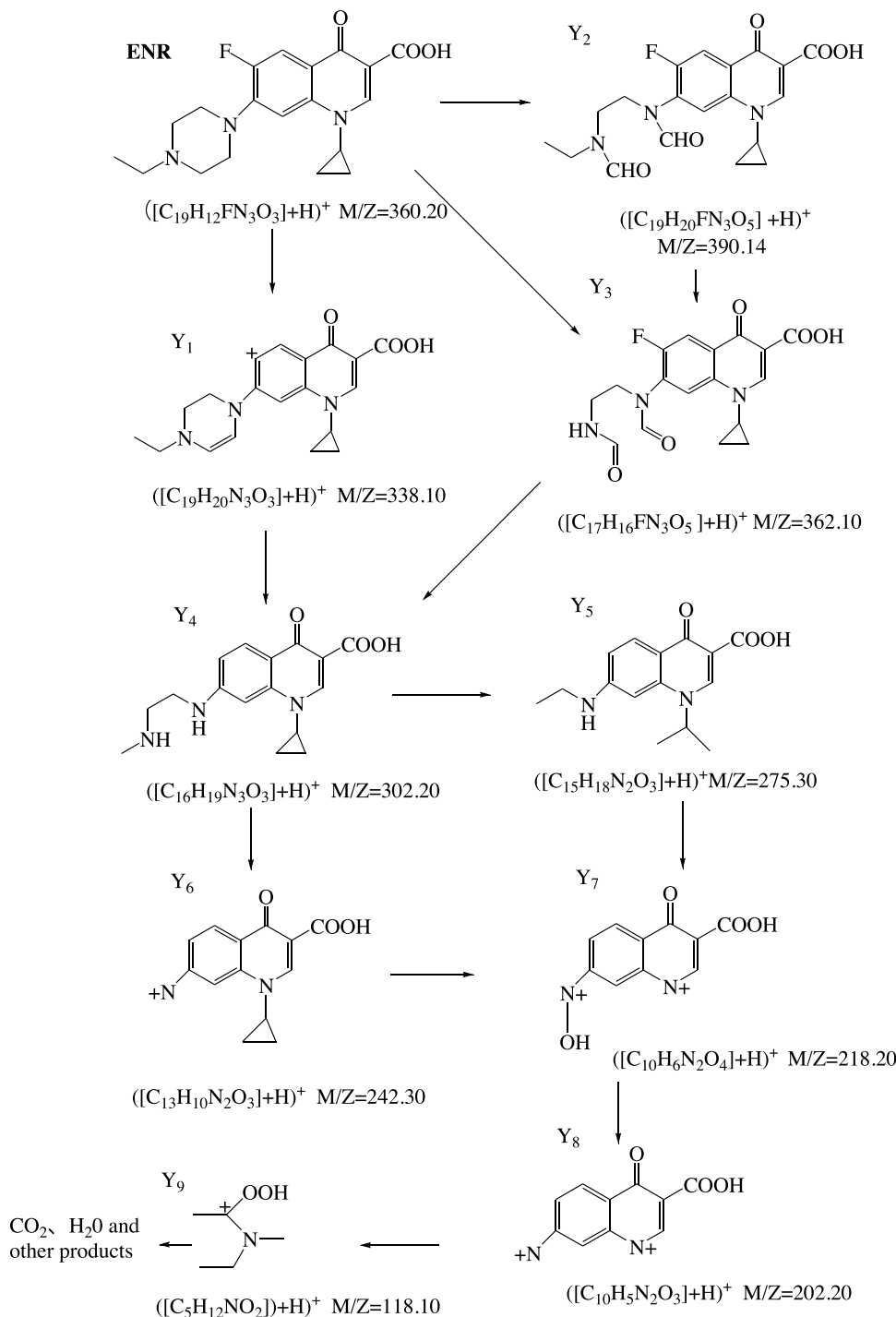


Scheme 2. Proposed degradation pathways of OTC by $\text{Ag}_3\text{PO}_4/\text{TiO}_2@\text{MoS}_2$ (3.5 wt%).

3.5. Proposed mechanism

In order to further investigate the photocatalytic degradation mechanism, the trapping experiments of $\text{Ag}_3\text{PO}_4/\text{TiO}_2@\text{MoS}_2$ (3.5 wt%) composite were conducted to determine the main

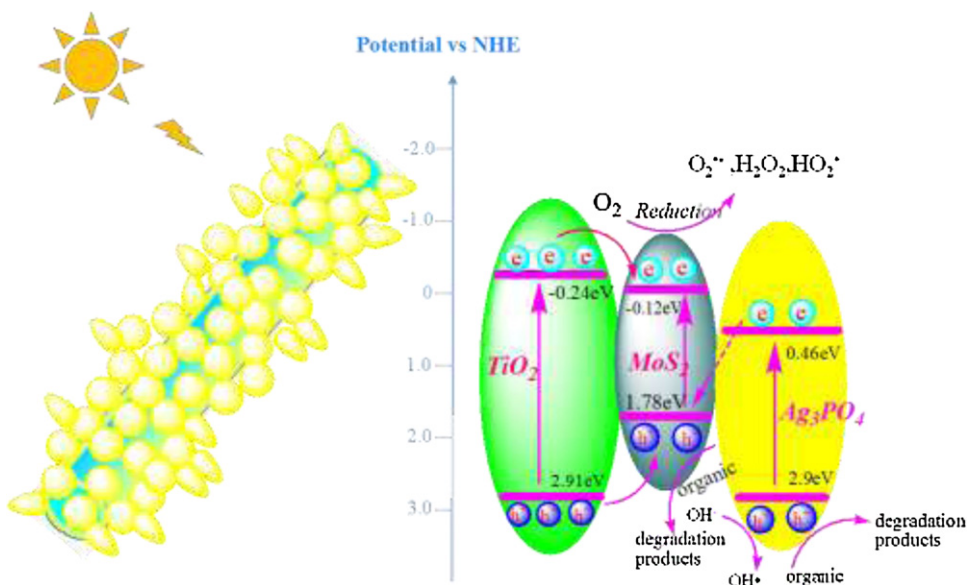
reactive species. In this study, ethylenediamine tetraacetic acid disodium salt (EDTA-2Na) and *tert*-butanol served as the hole (h^+) scavenger and hydroxyl radical ($\cdot\text{OH}$) scavenger, respectively. *tert*-butyl alcohol and EDTA-2Na show the different influence on photocatalysis degradation interestingly (Fig. 10). *tert*-butyl alco-



Scheme 3. Proposed degradation pathways of ENR by Ag₃PO₄/TiO₂@MoS₂ (3.5 wt%).

hol almost did not show any inhibitory effect on photodegradation of OTC and ENR, while EDTA-2Na significantly inhibited the photodegradation of OTC and ENR. As EDTA-2Na was added in reactor, the degradation rate of OTC and ENR dropped by 42% and 53% compared with the blank value, respectively. The results demonstrated that photogenerated holes were the main active oxidizing species involved in the photoreaction process. This conclusion might provide a new idea to transfer more holes from the core of photocatalyst to the surface. We might consider it as a simple and efficient way to improve the photocatalytic activity and anti-photocorrosion of photocatalysts. Thus, the control of morphology of Ag_3PO_4 will be further investigated in our future studies.

Based on the above research, a tentative photocatalytic degradation mechanism of 3D $\text{Ag}_3\text{PO}_4/\text{TiO}_2@\text{MoS}_2$ (3.5 wt%) is proposed (**Scheme 4**). Under Xe lamp illumination, the valence band (VB) electrons of Ag_3PO_4 are excited to the conduction band (CB), and then photogenerated electrons are immediately transferred to the valence band of MoS_2 through the surface contacts due to excellent electrical conductivity of MoS_2 . Meanwhile, the electrons of valence band of MoS_2 were excited to the conduction band, leading to the inhibition of the photogenerated carriers' recombination. Of course, some photogenerated electrons excited by a small amount of ultraviolet light in TiO_2 nanofibers could migrate to the conduction band of MoS_2 . Meanwhile, the $\text{TiO}_2@\text{MoS}_2$ heterostructure



Scheme 4. Schematic illustration of the energy band structure of the three-dimensional $\text{Ag}_3\text{PO}_4/\text{TiO}_2@\text{MoS}_2$ composites and the proposed charge mechanism.

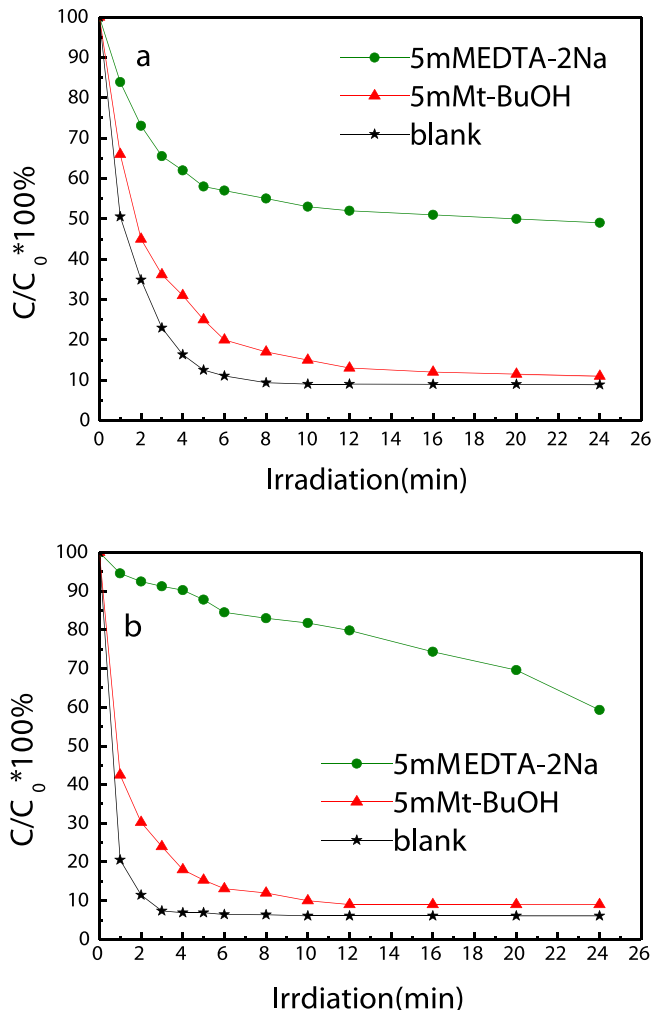


Fig. 10. Plots of photogenerated active species trapped in the system during photodegradation of (a) OTC and (b) ENR by $\text{Ag}_3\text{PO}_4/\text{TiO}_2@\text{MoS}_2$ (3.5 wt%) under Xe lamp irradiation.

composed of TiO_2 nanofibers frame could play the role of 'wire' to guide electrons captured by MoS_2 and transferred electrons into solution quickly. Subsequently, these electrons contacted with H_2O or O_2 in solution, accompanied by a series of free radical chain reaction, generated ' HO_2^{\cdot} ', ' $\text{O}_2^{\cdot-}$ ', etc. Since both CB and VB positions of MoS_2 are higher than that of TiO_2 , the h^+ could also be transferred from the VB of TiO_2 to the VB of MoS_2 . More importantly, the h^+ isolated could oxidize the organic pollutants and OH^- effectively. Thus, $\text{Ag}_3\text{PO}_4/\text{TiO}_2@\text{MoS}_2$ showed excellent photocatalytic degradation activity and anti-photocorrosion.

4. Conclusions

In summary, 3D $\text{Ag}_3\text{PO}_4/\text{TiO}_2@\text{MoS}_2$ composites with various contents of $\text{TiO}_2@\text{MoS}_2$ were successfully prepared via electrospinning, sequential hydrothermal reaction and chemical deposition. Enhanced visible light induced photocatalytic degradation performance of dyes and antibiotics were achieved over $\text{Ag}_3\text{PO}_4/\text{TiO}_2@\text{MoS}_2$ (3.5 wt%) and schemes of OTC and ENR photodegradation over $\text{Ag}_3\text{PO}_4/\text{TiO}_2@\text{MoS}_2$ were proposed. Upon irradiation by visible light, the photogenerated electrons in the conduction band of Ag_3PO_4 could be immediately transferred to the surface of $\text{TiO}_2@\text{MoS}_2$ heterostructure and subsequently reacted with H_2O , O_2 or OH^- in solution, resulting in transferring more holes from the core of photocatalyst to the surface. Radical trapping experiments demonstrated that the holes isolated from photocatalyst played important role in oxidative degradation of OTC and ENR, so that $\text{Ag}_3\text{PO}_4/\text{TiO}_2@\text{MoS}_2$ (3.5 wt%) showed higher photocatalytic degradation activity and anti-photocorrosion. After successive cycling runs, $\text{Ag}_3\text{PO}_4/\text{TiO}_2@\text{MoS}_2$ (3.5 wt%) could still remain high photodegradation rate of target pollutants. Thus, $\text{Ag}_3\text{PO}_4/\text{TiO}_2@\text{MoS}_2$ (3.5 wt%) is a promising photocatalyst for the removal of organic pollutants in the environmental protection. More importantly, this study provided a simple and efficient way to improve the photocatalytic activity and anti-photocorrosion of photocatalysts, which might be benefit to the environment remediation and purification processes.

Acknowledgements

This research was supported by Water Resource Project of Jiangsu Province (2016039) and Integration of Industry and Uni-

versity Research Funds of Jiangsu Province (BY2015060-2). We also acknowledge the generous support provided by Environmental Protection Research Funds of Jiangsu Province (2015010) and Major Program of National Natural Science fundation of China (No. 51438008).

Appendix A. Supplementary data

Supplementary data associated with this article can be found, in the online version, at <http://dx.doi.org/10.1016/j.apcatb.2016.11.008>.

References

- [1] F. Teng, Z. Liu, A. Zhang, M. Li, Environ. Sci. Technol. 49 (2015) 9489–9494.
- [2] E. Bailón-García, A. Elmouwahidi, M.A. Álvarez, F. Carrasco-Marín, A.F. Pérez-Cadenas, F.J. Maldonado-Hódar, Appl. Catal. B: Environ. 201 (2017) 29–40.
- [3] L. Wang, Y. Chai, J. Ren, J. Ding, Q. Liu, W.L. Dai, Dalton Trans. 44 (2015) 14625–14634.
- [4] C. Tang, E. Liu, J. Wan, X. Hu, J. Fan, Appl. Catal. B: Environ. 181 (2016) 707–715.
- [5] Z.-M. Yang, Y. Tian, G.-F. Huang, W.-Q. Huang, Y.-Y. Liu, C. Jiao, Z. Wan, X.-G. Yan, A. Pan, Mater. Lett. 116 (2014) 209–211.
- [6] X. Hua, Y. Jin, K. Wang, N. Li, H. Liu, M. Chen, S. Paul, Y. Zhang, X. Zhao, F. Teng, Catal. Commun. 52 (2014) 49–52.
- [7] P. Dong, Y. Wang, H. Li, H. Li, X. Ma, L. Han, J. Mater. Chem. A 1 (2013) 4651.
- [8] Y. Lv, K. Huang, W. Zhang, B. Yang, F. Chi, S. Ran, X. Liu, Ceram. Int. 40 (2014) 8087–8092.
- [9] J. Liu, X. Li, F. Liu, L. Lu, L. Xu, L. Liu, W. Chen, L. Duan, Z. Liu, Catal. Commun. 46 (2014) 138–141.
- [10] X. Chen, Y. Dai, J. Guo, T. Liu, X. Wang, Ind. Eng. Chem. Res. 55 (2016) 568–578.
- [11] A. Samal, D.P. Das, K.K. Nanda, B.K. Mishra, J. Das, A. Dash, Chem.-Asian. J. 11 (2016) 584–595.
- [12] N. Wang, Y. Zhou, C. Chen, L. Cheng, H. Ding, Catal. Commun. 73 (2016) 74–79.
- [13] X. Lin, X. Guo, W. Shi, F. Guo, G. Che, H. Zhai, Y. Yan, Q. Wang, Catal. Commun. 71 (2015) 21–27.
- [14] Y. Bu, Z. Chen, C. Sun, Appl. Catal. B: Environ. 179 (2015) 363–371.
- [15] Y. Bu, Z. Chen, C. Sun, Appl. Catal. B: Environ. 198 (2016) 347–377.
- [16] L. Liu, Y. Qi, J. Lu, S. Lin, W. An, Y. Liang, W. Cui, Appl. Catal. B: Environ. 183 (2016) 133–141.
- [17] M. Chhowalla, H.S. Shin, G. Eda, L.J. Li, K.P. Loh, H. Zhang, Nat. Chem. 5 (2013) 263–275.
- [18] H. Wang, H. Feng, J. Li, Small 10 (2014) 2165–2181.
- [19] Y. Liu, Y.-X. Yu, W.-D. Zhang, J. Phys. Chem. C 117 (2013) 12949–12957.
- [20] M. Shen, Z. Yan, L. Yang, P. Du, J. Zhang, B. Xiang, Chem. Commun. 50 (2014) 15447–15449.
- [21] J. Di, J. Xia, Y. Ge, L. Xu, H. Xu, J. Chen, M. He, H. Li, Dalton. Trans. 43 (2014) 15429–15438.
- [22] J. Li, K. Yu, Y. Tan, H. Fu, Q. Zhang, W. Cong, C. Song, H. Yin, Z. Zhu, Dalton Trans. 43 (2014) 13136–13144.
- [23] Y. Chen, G. Tian, Y. Shi, Y. Xiao, H. Fu, Appl. Catal. B: Environ. 164 (2015) 40–47.
- [24] X. Yang, J. Qin, Y. Jiang, K. Chen, X. Yan, D. Zhang, R. Li, H. Tang, Appl. Catal. B: Environ. 166–167 (2015) 231–240.
- [25] D. Wang, Z. Li, L. Shang, J. Liu, J. Shen, Thin Solid Films 551 (2014) 8–12.
- [26] Y. Song, Y. Lei, H. Xu, C. Wang, J. Yan, H. Zhao, Y. Xu, J. Xia, S. Yin, H. Li, Dalton Trans. 44 (2015) 3057–3066.
- [27] C. Liu, L. Wang, Y. Tang, S. Luo, Y. Liu, S. Zhang, Y. Zeng, Y. Xu, Appl. Catal. B: Environ. 164 (2015) 1–9.
- [28] J. Li, Z. Guo, Z. Liu, M. Cui, Z. Zhu, Phys. Status Solidi A 212 (2015) 459–466.
- [29] Y. Li, L. Yu, N. Li, W. Yan, X. Li, J. Colloid Interface Sci. 450 (2015) 246–253.
- [30] X. Ma, H. Li, Y. Wang, H. Li, B. Liu, S. Yin, T. Sato, Appl. Catal. B: Environ. 158–159 (2014) 314–320.
- [31] X. Wang, M. Utsumi, Y. Yang, D. Li, Y. Zhao, Z. Zhang, C. Feng, N. Sugiura, J.J. Cheng, Appl. Surf. Sci. 325 (2015) 1–12.
- [32] J. Xie, Y. Yang, H. He, D. Cheng, M. Mao, Q. Jiang, L. Song, J. Xiong, Appl. Surf. Sci. 355 (2015) 921–929.
- [33] L. Yang, W. Duan, H. Jiang, S. Luo, Y. Luo, Mater. Res. Bull. 70 (2015) 129–136.
- [34] S. Li, X. Gu, Y. Zhao, Y. Qiang, S. Zhang, M. Sui, J. Mater. Sci.—Mater. Electron. 27 (2015) 386–392.
- [35] Y. Chen, C. Hu, J. Qu, M. Yang, J. Photochem. Photobiol. A 197 (2008) 81–87.
- [36] I. Dalmasio, M.O. Almeida, R. Augusti, T.M. Alves, J. Am. Soc. Mass. Spectrom. 18 (2007) 679–687.
- [37] P. Huo, Z. Lu, X. Liu, D. Wu, X. Liu, J. Pan, X. Gao, W. Guo, H. Li, Y. Yan, Chem. Eng. J. 189–190 (2012) 75–83.
- [38] G. Jácome-Acatitla, F. Tzompantzi, R. López-González, C. García-Mendoza, J.M. Alvaro, R. Gómez, J. Photochem. Photobiol. A 277 (2014) 82–89.
- [39] J. Jeong, W. Song, W.J. Cooper, J. Jung, J. Greaves, Chemosphere 78 (2010) 533–540.
- [40] S. Jiao, S. Zheng, D. Yin, L. Wang, L. Chen, J. Environ. Sci. 20 (2008) 806–813.
- [41] S. Jiao, S. Zheng, D. Yin, L. Wang, L. Chen, Chemosphere 73 (2008) 377–382.
- [42] R. Li, Y. Jia, J. Wu, Q. Zhen, RSC Adv. 5 (2015) 40764–40771.
- [43] Z. Lu, P. Huo, Y. Luo, X. Liu, D. Wu, X. Gao, C. Li, Y. Yan, J. Mol. Catal. A: Chem. Chem. 378 (2013) 91–98.
- [44] H. Sanderson, F. Ingerslev, R.A. Brain, B. Halling-Sorensen, J.K. Bestari, C.J. Wilson, D.J. Johnson, K.R. Solomon, Chemosphere 60 (2005) 619–629.
- [45] F. Yuan, C. Hu, X. Hu, D. Wei, Y. Chen, J. Qu, J. Hazard. Mater. 185 (2011) 1256–1263.
- [46] S. Babic, M. Perisa, I. Skoric, Chemosphere 91 (2013) 1635–1642.
- [47] D. Dolar, K. Košutić, M. Periša, S. Babić, Sep. Purif. Technol. 115 (2013) 1–8.
- [48] Z. Lu, F. Chen, M. He, M. Song, Z. Ma, W. Shi, Y. Yan, J. Lan, F. Li, P. Xiao, Chem. Eng. J. 249 (2014) 15–26.
- [49] A. Speltini, M. Sturini, F. Maraschi, A. Profumo, A. Albini, TrAC. Trends Anal. Chem. 30 (2011) 1337–1350.
- [50] A. Speltini, M. Sturini, F. Maraschi, A. Profumo, A. Albini, Anal. Bioanal. Chem. 404 (2012) 1565–1569.
- [51] M. Sturini, A. Speltini, F. Maraschi, L. Pretali, A. Profumo, E. Fasani, A. Albini, Environ. Sci. Pollut. R 21 (2014) 13215–13221.
- [52] M. Sturini, A. Speltini, F. Maraschi, L. Pretali, A. Profumo, E. Fasani, A. Albini, R. Migliavacca, E. Nucleo, Water Res. 46 (2012) 5575–5582.
- [53] M. Sturini, A. Speltini, F. Maraschi, A. Profumo, L. Pretali, E. Fasani, A. Albini, Chemosphere 86 (2012) 130–137.
- [54] M. Sturini, A. Speltini, F. Maraschi, A. Profumo, L. Pretali, E.A. Irastorza, E. Fasani, A. Albini, Appl. Catal. B: Environ. 119–120 (2012) 32–39.
- [55] M. Sturini, A. Speltini, F. Maraschi, E. Rivagli, L. Pretali, L. Malavasi, A. Profumo, E. Fasani, A. Albini, J. Photochem. Photobiol. A 299 (2015) 103–109.
- [56] R. Tao, G.G. Ying, H.C. Su, H.W. Zhou, J.P. Sidhu, Environ. Pollut. 158 (2010) 2101–2109.
- [57] K.H. Wammer, A.R. Korte, R.A. Lundein, J.E. Sundberg, K. McNeill, W.A. Arnold, Water Res. 47 (2013) 439–448.